



<b>Publication Year</b>	2016
<b>Acceptance in OA</b>	2020-05-13T09:18:04Z
<b>Title</b>	Polarimetric analysis of a CdZnTe spectro-imager under multi-pixel irradiation conditions
<b>Authors</b>	Pinto, M., da Silva, R. M. Curado, Maia, J. M., Simões, N., Marques, J., Pereira, L., Trindade, A. M. F., CAROLI, EZIO, AURICCHIO, NATALIA, STEPHEN, JOHN BUCHAN, Gonçalves, P.
<b>Publisher's version (DOI)</b>	10.1016/j.nima.2016.09.054
<b>Handle</b>	<a href="http://hdl.handle.net/20.500.12386/24780">http://hdl.handle.net/20.500.12386/24780</a>
<b>Journal</b>	NUCLEAR INSTRUMENTS & METHODS IN PHYSICS RESEARCH. SECTION A, ACCELERATORS, SPECTROMETERS, DETECTORS AND ASSOCIATED EQUIPMENT
<b>Volume</b>	840

# Polarimetric analysis of a CdZnTe spectro-imager under multi-pixel irradiation conditions

M. Pinto<sup>a,b</sup>, R.M. Curado da Silva<sup>a,b,\*</sup>, J.M. Maia<sup>a,c</sup>, N. Simões<sup>a,b</sup>, J. Marques<sup>a,d</sup>, L. Pereira<sup>a</sup>, A.M.F. Trindade<sup>a</sup>, E. Caroli<sup>e</sup>, N. Auricchio<sup>e</sup>, J.B. Stephen<sup>e</sup>, P. Gonçalves<sup>a</sup>

<sup>a</sup> LIP-Laboratório de Instrumentação e Física Experimental de Partículas, Portugal

<sup>b</sup> Physics Department, University of Coimbra, Coimbra, Portugal

<sup>c</sup> Physics Department, University of Beira-Interior, Covilhã, Portugal

<sup>d</sup> Centro de Astrofísica, Universidade do Porto, Porto, Portugal

<sup>e</sup> INAF-IASF-Bologna, Bologna, Italy

---

## ARTICLE INFO

*Keywords:*  
Polarimetry  
X-rays  
Gamma-rays  
CdZnTe  
Astrophysics  
Detectors

## ABSTRACT

So far, polarimetry in high-energy astrophysics has been insufficiently explored due to the complexity of the required detection, electronic and signal processing systems. However, its importance is today largely recognized by the astrophysical community, therefore the next generation of high-energy space instruments will certainly provide polarimetric observations, contemporaneously with spectroscopy and imaging. We have been participating in high-energy observatory proposals submitted to ESA Cosmic Vision calls, such as GRI (Gamma-Ray Imager), DUAL and ASTROGAM, where the main instrument was a spectro-imager with polarimetric capabilities. More recently, the H2020 AHEAD project was launched with the objective to promote more coherent and mature future high-energy space mission proposals. In this context of high-energy proposal development, we have tested a CdZnTe detection plane prototype polarimeter under a partially polarized gamma-ray beam generated from an aluminum target irradiated by a <sup>22</sup>Na (511 keV) radioactive source. The polarized beam cross section was 1 cm<sup>2</sup>, allowing the irradiation of a wide multi-pixelated area where all the pixels operate simultaneously as a scatterer and as an absorber. The methods implemented to analyze such multi-pixel irradiation are similar to those required to analyze a spectro-imager polarimeter operating in space, since celestial source photons should irradiate its full pixelated area. Correction methods to mitigate systematic errors inherent to CdZnTe and to the experimental conditions were also implemented. The polarization level (~40%) and the polarization angle (precision of ±5° up to ±9°) obtained under multi-pixel irradiation conditions are presented and compared with simulated data.

---

## 1. Introduction

Polarimetry in high-energy astrophysics has been insufficiently explored due to the complexity of the required detection, electronic and signal processing systems, since celestial gamma-ray sources are only observable by high-altitude balloon or satellite missions in space. To date, no dedicated gamma-ray polarimeters have been launched into space. X- and gamma-ray source emissions have been studied almost exclusively through spectral and timing analysis of the measured fluxes and by using imaging techniques based on coded-mask cameras or telescopes equipped with high efficiency focal plane detectors. Polarization measurements will increase the number of observational parameters of a gamma-ray source by two: the polarization angle and the level of linear polarization. These additional

parameters should allow a better discrimination between different emission models characterizing the same object. Polarimetric observations can provide important information about the geometry, the magnetic field, the composition and the emission mechanisms. Polarized emissions are expected in a wide variety of gamma-ray sources such as pulsars, solar flares, active galactic nuclei, galactic black-holes and gamma-ray bursts [1–3]. In the soft X-ray domain (< 10 keV) two observations performed in the 1970's by a rocket flight and by the OSO-8 (Orbiting Solar Observatory) polarimeter measured the Crab Nebula polarization [4,5]. In the soft gamma-ray domain (100 keV to 1 MeV), although some dedicated polarimeters have been proposed [6–14], only a few polarimetric measurements were performed by the SPI (Spectrometer On INTEGRAL) and IBIS (Imager on Board the INTEGRAL Satellite) instruments onboard the INTEGRAL

---

\* Corresponding author at: LIP-Laboratório de Instrumentação e Física Experimental de Partículas, Universidade de Coimbra, P-3004-516 Coimbra, Portugal.  
E-mail address: rui.silva@coimbra.lip.pt (R.M.C. da Silva).

(INTERNational Gamma-Ray Astrophysics Laboratory) mission [15,16], on the Crab Pulsar, on the galactic black-hole Cygnus X-1 and on the gamma-ray burst GRB 041219A [17–20].

The importance of polarimetry is today largely recognized by the high-energy astrophysical community. Therefore, the next generation of telescopes should certainly provide polarimetric observations, contemporaneously with spectroscopy and imaging. These multipurpose instrument types were proposed in recent high-energy (100 keV to 1 GeV) space mission concepts submitted to ESA Cosmic Vision calls where our groups were proposal partners, such as: the GRI (Gamma-Ray Imager), DUAL and ASTROGAM [21–23]. In the framework of these space mission proposals, we have been studying, developing and proposing different configuration detection plane prototypes for high-energy polarimetry. These prototypes were semiconductor based (mostly CdTe family) detection planes designed for coded mask or for Laue lens instrument solutions. These solutions require a trade-off between the imaging, spectroscopy and polarimetry components [24,25] that depends on the mission scientific objectives and which results in a substantially different configuration than those required for dedicated polarimeters [7,14,25]. So far there has been insufficient interest from the space agencies (including ESA) of our countries to accept a dedicated Compton polarimeter. The broader scientific return of a multipurpose mission (imaging, spectrometry and polarimetry) is often regarded as a better choice, in spite of its additional cost when compared with a simple dedicated polarimeter mission.

LIP (Laboratório de Instrumentação e Física Experimental de Partículas), Coimbra, Portugal is a partner in the Horizon 2020 AHEAD (Activities in the High Energy Astrophysics Domain) project (H2020 EU ref.: 654215) started in September 2015. The main objective of AHEAD is to promote synergies between the distinct national efforts in high-energy astrophysics in order to provide more coherent and mature future space observatory joint proposals to future ESA calls for missions. Therefore our main objective in polarimeter development is mostly associated with multipurpose innovative instruments that can provide a sensitivity increase in the high-energy domain. Although the experiment described herein was performed before the AHEAD project approval, the main purpose of this work is to contribute to optimize the polarimetric performances of future high-energy space proposals. Within this scope, a CdZnTe (CZT) polarimeter prototype was tested under a partially polarized gamma-rays beam generated by Compton scattering on a low-Z target irradiated by a  $^{22}\text{Na}$  (511 keV) radioactive source. These measurements were performed in a polarimetry dedicated workbench at LIP laboratory, following a series of experiments carried out at the ESRF (European Synchrotron Radiation Facility) under a polarized synchrotron gamma-rays beam in the 100–750 keV range [27–32]. In these previous synchrotron beam experiments, the beam was collimated to impinge within a single pixel detector area ( $2 \times 2 \text{ mm}^2$ ) due to beam diameter technical limitations. Another limitation of the ESRF polarized gamma-rays beam was the exponentially decreasing beam flux as the level of polarization was reduced. Since the number of beam slots available at the ESRF is limited for an experiment session period, generally it was not envisaged to perform measurements for beam polarization levels lower than 80%. In the LIP laboratory we are not subject to this restriction, therefore we were able to reproduce an irradiation configuration closer to in-flight observational conditions. Since celestial source emissions are partially polarized and since the flux irradiates the instrument's full detection plane surface, we tested the CZT prototype under a partially polarized beam (from ~65% down to ~40%) that irradiated multiple detector pixels simultaneously with a total area of  $\sim 1 \text{ cm}^2$ . Therefore, instead of previously tested irradiation conditions such as central matrix pixel scatterer or scatterer-calorimeter configurations [26–38], we irradiated a large active detection surface where all the detection units (pixels) operated simultaneously as a scatterer and as an absorber. The results obtained are discussed and compared with previous single pixel irradiation polarimetric experiments. In particular, we describe multi-

ple pixel irradiation analysis as well as correction methods to mitigate the CZT matrix inherent systematic errors affecting the polarimetric response.

## 2. Compton polarimetry

The polarimetric performance of a high-energy detection plane is determined by the fundamental concepts associated with polarized Compton interactions and by its design. The Compton scattering of a polarized photon beam generates non-uniformity in the azimuthal angular distribution of the scattered photons. The scattered photon's angular direction depends on its initial polarization angle. If the scattered photon goes through a new interaction inside the detector, the statistical distribution of photons's angular directions defined by the two interactions (double-event) provides a modulation curve from which the degree and polarization direction of the incident beam can be derived. The azimuthal angular distribution of the scattered photons is given by the Klein-Nishina differential cross-section for linearly polarized photons:

$$\frac{d\sigma}{d\Omega} = \frac{r_0^2}{2} \left( \frac{E'}{E} \right)^2 \left[ \frac{E'}{E} + \frac{E}{E'} - 2 \sin^2 \theta \cos^2 \phi \right], \quad (1)$$

where  $r_0$  is the classical electron radius,  $E$  and  $E'$  are, respectively, the energies of the incoming and outgoing photons,  $\theta$  the angle of the scattered photons and  $\phi$  is the angle between the scattering plane (defined by the incoming and outgoing photon directions) and incident polarization plane (defined by the polarization direction and the direction of the incoming photon). As can be seen from (1), after fixing all other parameters the scattering probability varies with the azimuthal angle  $\phi$  and its maximum and minimum arises for orthogonal directions. For  $\phi=0^\circ$  the cross-section reaches a minimum and for  $\phi=90^\circ$  the cross-section reaches a maximum. However, this relative difference is maximized for a scattering angle  $\theta_M$ , dependent on the incident photon energy. For soft  $\gamma$ - and hard X-rays (0.1–1 MeV) the  $\theta_M$  value is about  $90^\circ$ . Note that  $E$  and  $E'$  are related by:

$$\frac{E'}{E} = \frac{1}{1 + \frac{E}{m_0 c^2} (1 - \cos \theta)}, \quad (2)$$

where  $c$  is the speed of light in free space and  $m_0$  is the electron rest mass.

The polarimetric performance of an instrument can be evaluated by calculating the polarimetric modulation factor,  $Q_{100}$ , of double-event distribution generated by a 100% polarized beam. For the case of a planar pixelated detector,  $Q_{100}$  can be calculated from the modulation curve resulting from a double-event angular distribution around a central irradiated pixel:

$$Q_{100} = \frac{N_{//} - N_{\perp}}{N_{//} + N_{\perp}}, \quad (3)$$

where  $N_{//}$  and  $N_{\perp}$ , are the double-events integrated over two orthogonal directions defined over the detector plane along the maxima and minima of the modulation curve [39].

## 3. Experimental setup and methods

This experimental study was performed with a polarimeter prototype based on a 5.0 mm thick IMARAD CZT ( $\text{Cd}_{0.9}\text{Zn}_{0.1}\text{Te}$ ) detector. The detector matrix was divided into  $16 \times 16$  pixels with an area of  $2.0 \text{ mm} \times 2.0 \text{ mm}$  each and with a 0.5 mm gap between consecutive pixels. Due to electronic constraints only 16 pixels (in  $4 \times 4$  configuration) could be read in coincidence. Therefore the total sensitive area available for the polarimetric measurements – that require coincidence electronics – was  $1.0 \text{ cm} \times 1.0 \text{ cm}$ . The detector was operated at room temperature with a bias voltage of 600 V (Fig. 1).

The signals generated by the 16 pixels were read by the front-end

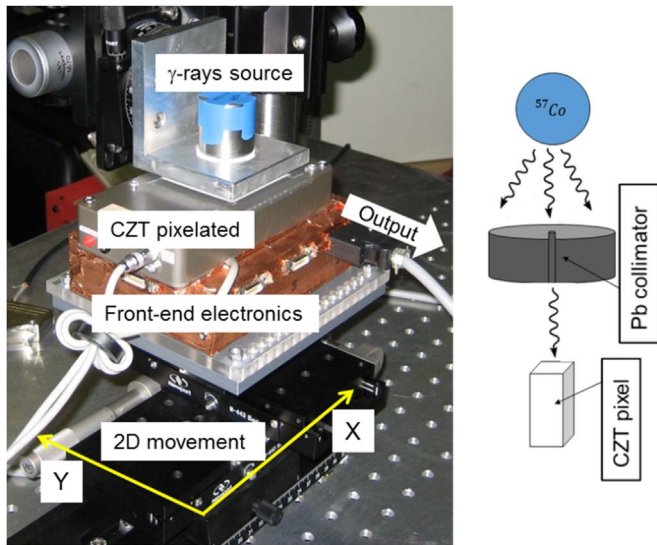


**Fig. 1.** The experimental setup for pixels's uniformity measurements (left) and schematic configuration of a single pixel irradiation (right). The CZT pixelated detector was mounted on a support that provides 2D movement.

electronics based on eight 16 channel eV-Products Application Specific Integrated Circuits (ASIC). Each channel consists of a charge sensitive amplifier followed by an active semi-Gaussian shaper (peaking-time of 1.2  $\mu$ s). Then the signals were processed by a custom multi-parametric system (named TAKES) consisting of 16 channels with filters, coincidence logic, analogue multiplexer and 10-bit Wilkinson type ADC units [27–31]. The TAKES system allows the pixel identification and energy measurement for each interaction in the CZT volume once the energy threshold for each interaction ( $\sim$ 40 keV) and the time coincidence window (2  $\mu$ s) are set. The coincidence logic is indispensable to select double-event detector hits and therefore to obtain the polarized beam modulation from the double-event distribution in the matrix

plane. The digital data were further processed and analyzed by a PC-based data acquisition (DAQ) system, which is based on a National Instruments PCI-6533 board with 32 parallel digital inputs/outputs. The DAQ was controlled by an algorithm written in LabView for Windows, allowing data manipulation, storage on the PC's hard-disk and data quick look on the PC's screen (Fig. 2).

The experimental study procedure required two different setups: (1) a setup for prototype intensity non-uniformity correction and (2) a setup for the CZT polarimetric measurements. In general the individual pixels' response inside the same CZT matrix is not uniform – it can vary up to 20% in the record number of counts for this prototype – due to material crystalline imperfections, non-uniformities that distort the internal electric field, carrier traps, etc. Thus, with the purpose of correcting the non-uniformity in pixel response, the CZT prototype was tested in the first experimental setup. A 3.0 cm thick lead collimator with a 0.7 mm diameter hole was placed between a  $\sim$ 50  $\mu$ Ci  $^{57}\text{Co}$  source (122 keV) and the detector, as is shown in Fig. 1. The detector was fixed to a mechanical support on a workbench allowing 2D movement with micrometric accuracy to direct the gamma-ray beam on the pixels and pixel centering. For each matrix pixel the number of interactions during 100 s acquisition time was recorded. From analysis of the measured pixels' response, the most uniform and less noisy 4 $\times$ 4 pixels set was chosen. This region is highlighted in Fig. 3 with its intensity map (recorded counts per pixel). The obtained 4 $\times$ 4 response matrix was recorded and used afterwards in the single-event correction method applied to the polarimetric measurements and analysis. Previous single-event corrections in single pixel irradiation ESRF experiments [27–31] showed that the energy dependence of the response matrix of this same prototype is relatively low for different energies up to 300 keV, varying up to  $\sim$ 5%. In this experiment, we similarly assumed low energy dependence when correcting non-uniformities of energy deposits (typically lower than 200 keV for double events) with a 122 keV  $^{57}\text{Co}$  source, the closest radioactive source energy available in the laboratory. Since the double-event flux produced by the source was comparable to the background double-

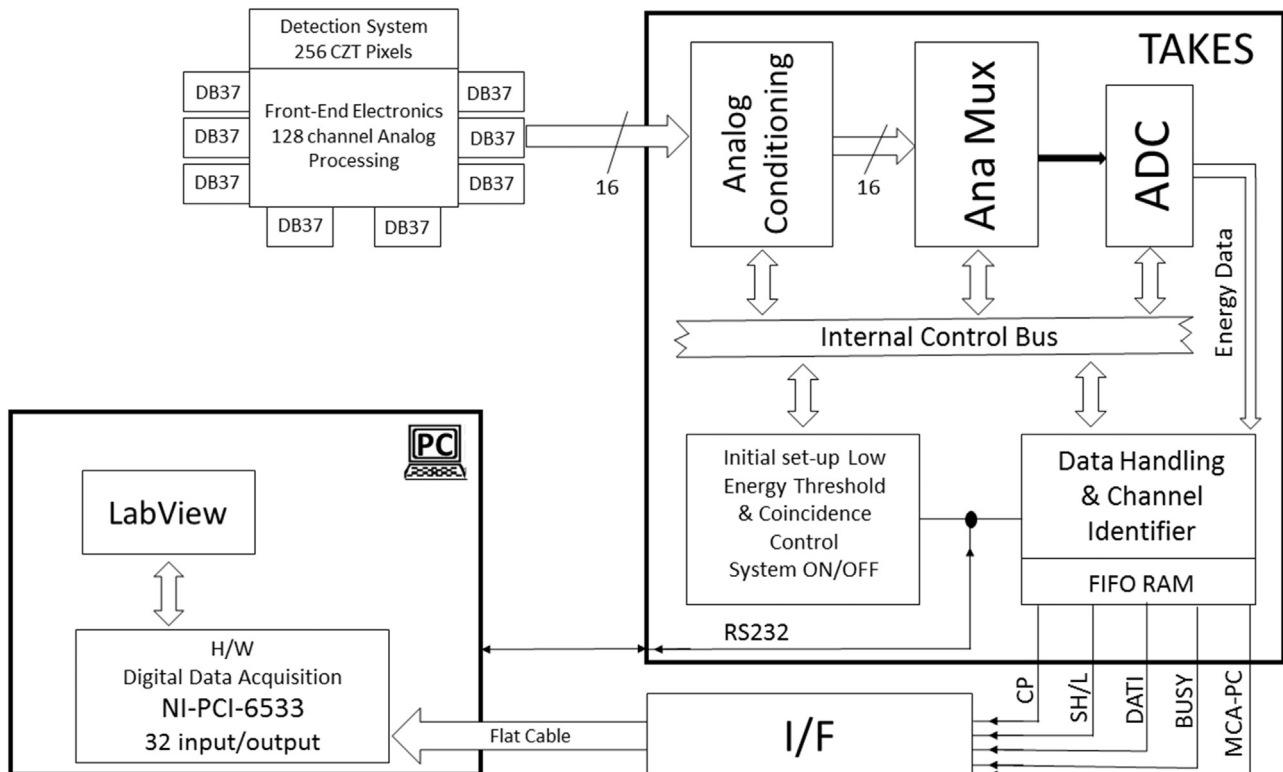


**Fig. 2.** Block diagram of the CZT pixelated detector electronic chain and DAQ system used in this work (see text for details).

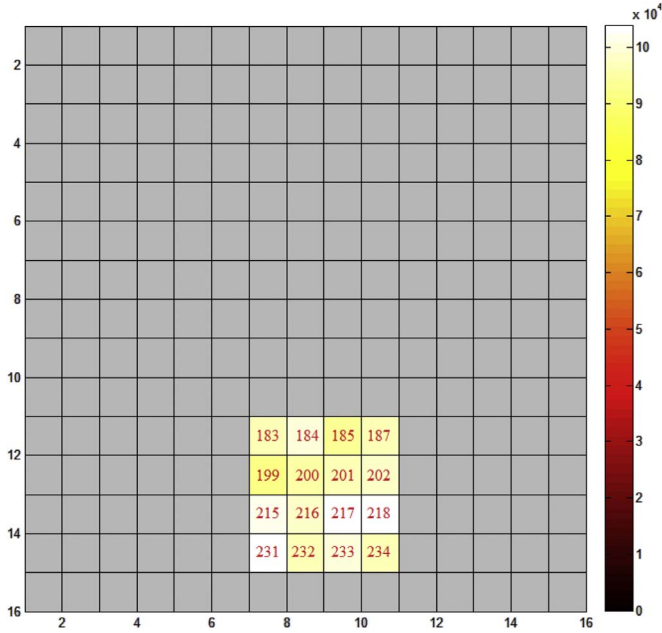


**Fig. 3.** Intensity map (recorded counts) obtained after irradiating each pixel in the same conditions. The red highlighted region contains the pixel numbers used in the polarimetric measurements. This restriction to 16 pixels was imposed by the number of electronic channels in coincidence available. Such pixels were chosen based on their disposition, uniformity in response and electronic noise magnitude.

events flux, for double-events whose hits combinations were distant in the matrix, implementing a correction method with unpolarized double-event offered a poor statistics and a mere second order correction:  $\sim 1\%$  to  $5\%$  results improvement, when compared with single events correction. The non-uniformity in the CZT matrix response is largely dominant. The referred ESRF experiments [27–31] provided similar conclusions when compared with double-event laboratory corrections.

The second experimental setup was designed to perform the polarimetric measurements (Fig. 4). The CZT matrix was irradiated by a large area ( $1.0 \text{ cm}^2$  square shape), partially polarized gamma-ray beam. A polarizer target was placed between an unpolarized  $\sim 18 \mu\text{Ci}$   $^{22}\text{Na}$  source and the CZT detector, forming a  $\sim 90^\circ$  oriented irradiation-detection geometry. Thus, a partially polarized gamma-ray beam is produced by Compton scattering of the incident  $511 \text{ keV}$  gamma-rays for scattering angles near  $90^\circ$ . It should be stressed that at this energy the maximum level of linear polarization which may be obtained is  $\sim 69\%$  at a scattering angle  $\sim 83^\circ$ , decreasing to  $\sim 67\%$  at a scattering angle  $\sim 90^\circ$  [1,34,35].

Nonetheless, the average level of linear polarization was calculated with a Monte-Carlo custom code developed in the C programming language. Moreover, the efficiency and the average energy for the photon beam arriving at the CZT plane were also calculated. NIST (National Institute of Standards and Technology) mass attenuation coefficients for the polarizer materials were used in the simulations [40]. A simplified model of our experimental setup was considered in the simulations: an unpolarized  $511 \text{ keV}$  photon collimated beam, with  $1.0 \text{ cm}$  diameter, irradiated centrally the polarizer target, whose flat surface forms an angle of  $45^\circ$  with the incident beam and with the perpendicular to the CZT plane. The CZT plane was centered with the polarizer target surface at a distance of  $10.0 \text{ cm}$ . The code tracked the photons path in the polarizer material, following the emerging photons trajectory that intersects the detection plane. From a simulated  $511 \text{ keV}$  photon beam an average level of linear polarization of  $\sim 65\%$  was obtained for a perfectly collimated incoming beam, but this was not the case in our experimental setup due to collimation shielding material constraints. In particular, in our setup the beam generated by

the source was of  $3.0 \text{ cm}$  diameter and there was a small distance of  $5.0 \text{ cm}$  between the  $^{22}\text{Na}$  source and the target, allowing angles between the incoming photons' trajectory and the axis source-target as large as  $\sim 35^\circ$  (see Fig. 4). The most peripheral photons interact with the polarizer target at scattering angles far-off  $90^\circ$ , generating an average polarization level of  $\sim 40\%$  [1]. If one considers all the possible angles then the resulting average polarization level of the beam generated by the target will be of  $\sim 50\%$ .

We considered three targets in our simulations, each having a cylindrical shape with  $3.0 \text{ cm}$  diameter and  $2.0 \text{ cm}$  thickness: plastic scintillator, aluminum and stainless steel. As presented in Table 1 the plastic scintillator provides the lower Compton efficiency, i.e. the percentage of incident photons that interact by Compton scattering, of  $\sim 1.49\%$ , while values of  $\sim 3.50\%$  and  $\sim 13.64\%$  were obtained for aluminum and stainless steel respectively. Furthermore, the ratio between the Compton photons that strike the detector active area and the incident photons were  $\sim 1.3 \times 10^{-3}\%$ ,  $\sim 3.2 \times 10^{-3}\%$  and  $\sim 1.1 \times 10^{-2}\%$ , respectively. However, it was verified that stainless steel generates  $\sim 25\%$  [multiple/(single+multiple)] of photons resulting from multiple interactions that reach the CZT plane, against only  $\sim 9\%$  for aluminum. These multiple interactions generated photons, that are nearly randomly polarized, blur the polarization information and contribute to an increase in the measured background noise. Therefore, we performed the polarimetric experiments only with the aluminum target since it provides a better balance between Compton efficiency and induced background noise level.

In the experimental setup, lead blocks shielded the CZT detector from photons coming directly from the source, also allowing an almost uniform irradiation of the detector active surface ( $\sim 1.0 \text{ cm}^2$ ). The limitations associated with the low efficiency of photons that hit the detector active area and the very low  $^{22}\text{Na}$  source activity results in quite long acquisition times ( $\sim 2 \times 10^5 \text{ s}$ ) to achieve enough statistics. Polarimetric measurements were performed for the aluminum target with the detector at angular positions of  $0^\circ$ ,  $45^\circ$  and  $90^\circ$ , relative to a horizontal reference axis, not necessarily coincident with the photons's polarization orientation, by rotating the detector prototype precision platform around its vertical axis (see Fig. 4).

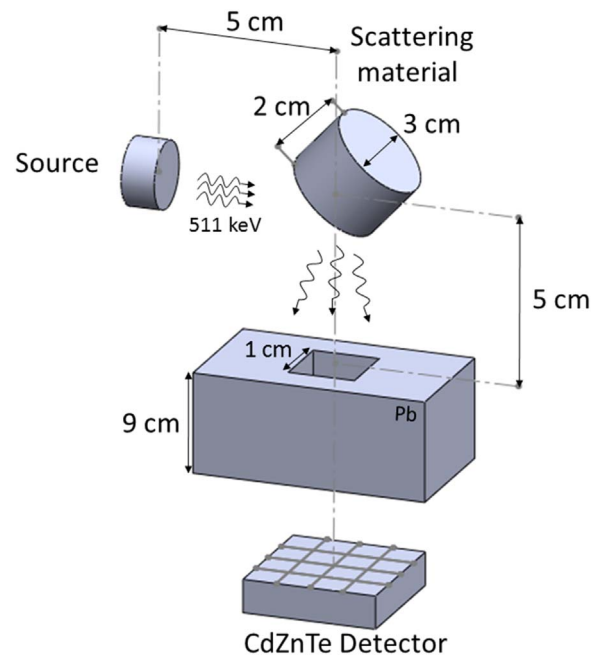


**Fig. 4.** Schematic configuration of the experimental polarimetric measurements' setup. A  $^{22}\text{Na}$  source emits  $511 \text{ keV}$  photons that will interact by Compton scattering on the polarizer target, resulting in partially polarized photon beam. The aperture between the polarizer and the detector allows wide active detector area irradiation ( $1 \text{ cm} \times 1 \text{ cm}$ ). The lead block also shields the detector from source direct photons.

**Table 1**  
Simulated beam parameters for target materials.

Parameter	Target		
	Plastic scintillator	Aluminum	Stainless-steel
Compton efficiency (%)	1.49	3.50	13.64
Multiple interactions (%)	0.066	0.34	4.64
Single interaction photons reaching the CZT plane (%)	$1.3 \times 10^{-3}$	$3.2 \times 10^{-3}$	$1.1 \times 10^{-2}$
Multiple interactions photons reaching the CZT plane (%)	$6.0 \times 10^{-5}$	$3.0 \times 10^{-4}$	$2.5 \times 10^{-3}$
Average energy (keV)	255.2	253.3	251.9

#### 4. Data correction and processing

There are several effects that introduce errors in the measurement process with consequences for the polarimetric modulation factor  $Q$  calculation. The most important of these effects is the non-uniformity in the matrix pixels' response (i.e. detection efficiency and intrinsic gain) due to material imperfections, traps, impurities, etc. However, other effects such as the tessellation of the pixelated matrix (squared in this case), which masks the polarization pattern by either enhancing or diminishing the level and angle of polarization measured, as well as the beam inclination and electronic noise may also affect the modulation factor  $Q$  calculation.

The procedure to correct the non-uniformity in the matrix pixels' response consisted firstly in irradiating uniformly the detector with an unpolarized gamma-ray beam (see section III). From this set of uniformity measurements a detector matrix response map for single events was obtained (see Fig. 3). The recorded fluctuations in the response between matrix pixels generate a residual modulation that will affect the polarimetric measurements. In order to correct for the non-uniformity in response during the polarimetric measurements, the number of recorded double interactions was replaced by the true number of double-events,  $N_{true}$ , in each irradiated pixel by applying the following relation:

$$N_{true} = \frac{N_{pol}}{N_{non}} N_{max}, \quad (4)$$

where  $N_{pol}$  is the number of double-events recorded in that pixel,  $N_{non}$  is the number of recorded single events in the same pixel obtained during the uniformity tests and  $N_{max}$  is the maximum number of single events obtained amongst all the matrix's pixels [1]. Furthermore, the double event matrix obtained when irradiating each pixel with such unpolarized beam, will be used to correct non-uniformities resulting from second hit distribution throughout the matrix, applying a similar methodology.

Instead of non-imaging polarimeters or single pixel irradiation polarimetric experiments, the irradiation of the full or extended pixelated detection plane, requires more complex polarimetric analysis. There are two methods to deal with simultaneous multi-pixel irradiation: a statistical method and a hit order reconstruction method. A statistical method that takes into account the  $\pi$  symmetry of polarized Compton photon angular distribution can be easily implemented when energy and order of the hits are not relevant [24]. Herein, we adopt the reconstruction method that allows determining the order of the hits in each double event. As stated previously, the Compton scattering angle  $\theta_M$  that maximizes  $Q$  in this energy range is  $\sim 90^\circ$ . In order to perform a fine  $\theta$  selection around  $90^\circ$ , it is important to identify the first and the second hit of a double-event. This method helps spurious coincidence rejection within the coincidence window, which is especially relevant under a low flux beam, as in this experiment. Furthermore, photon trajectory reconstruction methods are generally implemented in the

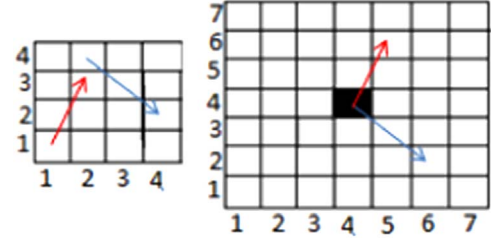


**Fig. 5.** Scheme representing the event reconstruction method when irradiating detector full surface. On the left side two events occurring in the  $4 \times 4$  matrix are displayed, one in red and one in blue. On the right side the reduction to a central pixel (the black one) is demonstrated. In the case of the red event the second interaction is taken to have occurred two pixels up and one to the right similar to the  $4 \times 4$  matrix. The blue event on the other hand had interactions in pixels separated by two pixels down and two to the right. (For interpretation of the references to color in this figure legend, the reader is referred to the web version of this article.)

imaging detection plane operation modes that we intend to develop. Since double-event hit signals are electronically simultaneous, it is necessary to take into account the Compton kinematics and the detector geometry to determine the order of each hit with a very high level of confidence. In this work, the recorded double interactions within the CZT detector occurred for Compton scattering angles around  $90^\circ$ . Since the photons emerge from the polarizer with energy around 255 keV (see Eq. (2)), the recorded double-events typically give rise to two distinct interactions, Compton and photoelectric, with energy deposited on the two pixels centered at  $\sim 85$  keV and  $\sim 170$  keV, respectively. It should be stressed that from the Compton scattering kinematics there is a very high probability that the first interaction occurs with a deposition of the lower energy and the second interaction with the higher energy [41]. Accordingly, in our algorithm, we selected as first interaction the hit generating a lower energy deposit and as second interaction the hit corresponding to the higher energy deposit. After determining the order of each double-event hit, we implemented a method where each double-event was projected in a central pixel of a virtual matrix. Fig. 5 illustrates this method: the first interaction of an event recorded in a  $4 \times 4$  matrix is processed as if it had occurred in the central pixel of a virtual  $7 \times 7$  matrix; the second one is then translated to the pixel in the same relative position as it occurred in the real  $4 \times 4$  matrix. With this method a double-event distribution centered on one pixel is obtained allowing trivial modulation curve building and  $Q$  modulation factor calculated from (3), when the beam irradiates multiple pixels in the focal plane. Besides, representing the double-events in maps also allows the visual identification of bad pixels or any other peculiarity that generates systematics or other effects that can have an impact on the modulation curve.

In order to minimize the contribution from background noise, mainly in the pixels where lower energy hits occur, energy band filters were applied to the acquired data. Thus only the data with energy within the ranges of 240–280 keV and 70–90 keV were selected, corresponding to the total energy and the first hit energy, respectively. The more restricted the selection range the better the modulation obtained, but the statistics significantly decrease so limiting this technique to applications with high flux emission.

In order to optimize the double-event histogram readout, we applied the radial bin technique (RBT) [1], by dividing the matrix into 24 radial bins of  $15^\circ$  each. Each double-event second hit was then assigned to a bin based on the pixel that detected it. Pixels partially crossed by angular bin lines contribute only with a fraction of the number of events equal to the fraction of its area that is in the sector - this is an approximation since real hits inside each pixel are not uniformly distributed but have a radial dependence relative to the position of the first Compton interaction of a double-event. The modulation curve,  $N(\phi)$ , giving the number of double-events as a function of the azimuthal angle, was then obtained. The polarimetric modulation factor  $Q$  was calculated from (3) and the polarization

direction was obtained from the angle that maximizes (3).

The described data correction and analysis techniques were implemented in a MatLab based code [42] that processed the prototype output data; the structure of the code is represented in Fig. 6. The first step for each hit is to check if it was detected in the same time coincidence window as another hit. In the second and third step the energy of both hits is compared with the values of the energy band filters, total energy and first hit energy. If the two double-event hits' energies lay inside both defined energy ranges then the event can be added to the double-event interaction matrix. Afterwards, we applied the RBT that provides the number of interactions in each angular bin, allowing polarimetric modulation factor  $Q$  and polarization angle calculation.

## 5. Results and discussion

Double-event intensity maps obtained with the aluminum target experimental setup of Fig. 4 are displayed in Fig. 7. These maps were obtained for relative polarization orientations of  $0^\circ$ ,  $45^\circ$  and  $90^\circ$ , by rotating the detector prototype precision platform around its vertical axis (see Fig. 4). The respective modulation curves are represented in Fig. 8(b)–(d), where the fitting curves in red are represented just for guideline purposes. The modulation factor  $Q$  obtained (see Table 2) for the different orientations ( $0^\circ$ ,  $45^\circ$  and  $90^\circ$ ) was consistently within the 0.11–0.12 range. The  $Q$  factor margin of error was calculated taking into account the error associated to the number of second hits recorded in each virtual pixel when integrated over the RBT independent bins and applying the error propagation formula to (3). In Fig. 8(a) is shown the residual modulation ( $Q_{res} = 0.021 \pm 0.004$ ) obtained by irradiating the detector with a 511 keV unpolarized gamma-ray beam. As can be seen in Fig. 8(a)–(d) there is a systematic peak effect with a  $90^\circ$  period. This can be explained by the obvious discontinuities that arise in the number of pixels inside the radial bins when applying the RBT at nearby diagonal directions ( $\sim 45^\circ$ ) to a squared pixel matrix with a very low level of pixelization ( $4 \times 4$  or virtual  $7 \times 7$ ) [27,31]. The magnitude of this spurious effect becomes more relevant as the pixelization level becomes lower. However, the objective of these measurements is to apply these techniques to high area and finer pixelization level spectro-imager polarimeters (at least  $32 \times 32$ ) [21] in broader energy bands (up to  $> 1$  MeV), with far more statistical data, especially for double-events generated by hits in distant pixels. In these conditions we expect this effect at  $\sim 45^\circ$  to become practically negligible [32].

The polarization level associated to the partially polarized beam modulation measurements was extrapolated from the ratio between the measured modulation  $Q$  factor and the  $Q_{100}$  factor obtained by a GEANT4 based simulation code [43]. This GEANT4 simulation program was previously extensively verified by a series of experimental measurements under a polarized beam generated at the ESRF [27–32]. In this code, the CZT prototype design was implemented simulating the experimental setup geometric conditions when irradiated by a 100% polarized beam with 255 keV incoming from the polarizer. When applying the same readout and analysis techniques to the simulated experiment, a modulation a  $Q_{100} = 0.30$  was obtained. Therefore, for an experimental factor  $Q$  measured within the 0.11–0.12 range, the corresponding measured level of polarization is almost 40% (Table 2). In section III the average level of linear polarization was estimated by a Monte-Carlo custom code, yielding a value of  $\sim 50\%$  for the photon beam emerging from the polarizer target. We used a custom code in the first stage of the photon's trajectory up to the polarizer in section III, instead of simulating the whole experiment with GEANT4 code, because GEANT4 photon's polarization angle orientation after a Compton scattering interaction was not validated experimentally, which is an essential parameter to simulate a second interaction in the CZT detector. Furthermore, the Monte-Carlo custom code provided more degrees of freedom to deal with all the parameters involved in this process. The difference between the simulated polarization level

and the measured experimental polarization level of  $\sim 40\%$  can be explained by the influence of environmental and system noise. In spite of the applied corrections described in chapter IV, fake coincidences were always present due to laboratorial environment background, electronic system noise and pixel response change with time. The noise generated by the background environment forced us to use a narrower window of energies that reduced the number of recorded events generated by the incident beam. Moreover, the low flux radiation sources available imposed long measurements, up to a couple of days ( $2 \times 10^5$  s), in order to obtain fair statistical data for all double-event combinations in the matrix. However, for double-events defined by distant pixel hits (peripheral pixels of the virtual  $7 \times 7$  matrix) the rate of beam generated double-events was of the same order of the rate of environment background generated double events. Furthermore, long measurements had the inconvenience of recording CZT pixels' time response variability (less than 5% variability up to 3 days [27–31]) and laboratorial environment background variability with an external vicinity origin that we could not control. As a consequence, we performed several measurements of the residual background modulation with the same time duration as polarized beam  $Q$  measurements ( $2 \times 10^5$  s), obtaining an average  $Q_{back}$ , of about 0.02 ( $\sim 7\%$  degradation of the polarization level), after data correction. Therefore, we can conclude that the modulation degradation (up to 7% less) of this factor on the beam final polarization level is consistent with the measured polarization of almost 40% and the respective margin of error ( $\pm 3\%$  up to  $\pm 6\%$ ).

Table 2 presents the measured polarization angle calculated when the detector axis was rotated by  $0^\circ$ ,  $45^\circ$  and  $90^\circ$  for an aluminum target. It can be seen that measured polarization angle is fairly consistent with the rotations performed on the system. Measured angles when the system is at  $0^\circ$  and  $90^\circ$  (note that this does not mean that the polarization direction is also exactly at these angles) were observed at about  $90^\circ$  apart within the measurement errors. At  $45^\circ$  the measured angle is slightly lower than expected. As described above, this can be explained by the limits of applying the RBT on the lower number of square pixels near  $45^\circ$  direction, because of the longer distance between separate pixel hits. Around  $45^\circ$ , scattered photons must cross more material to reach the most external pixels, i.e. a lower

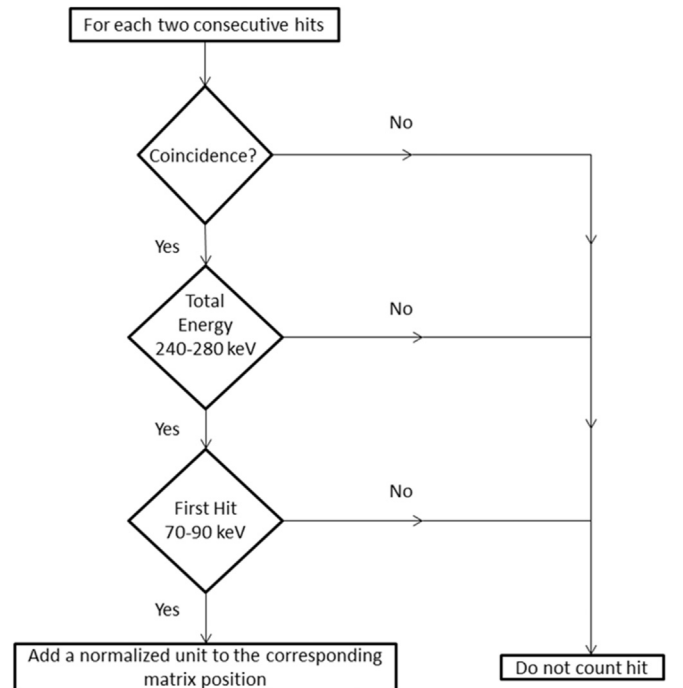
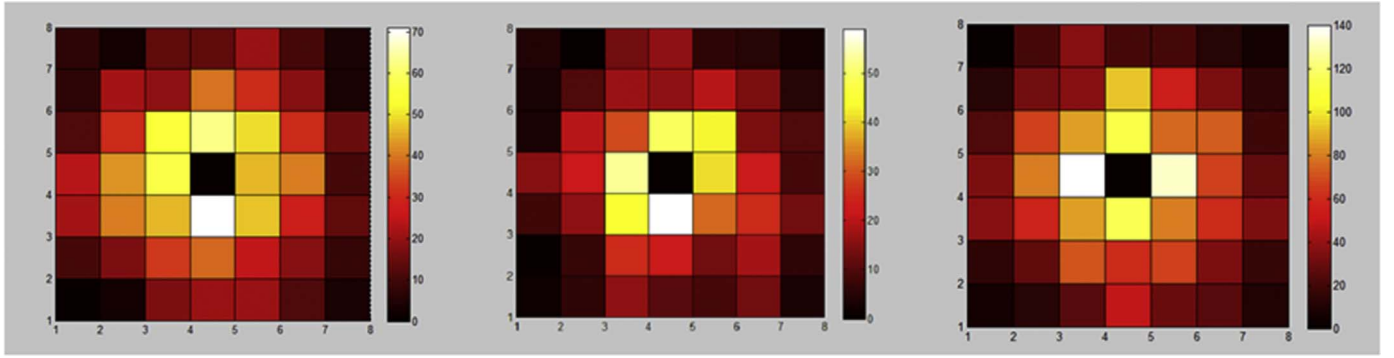
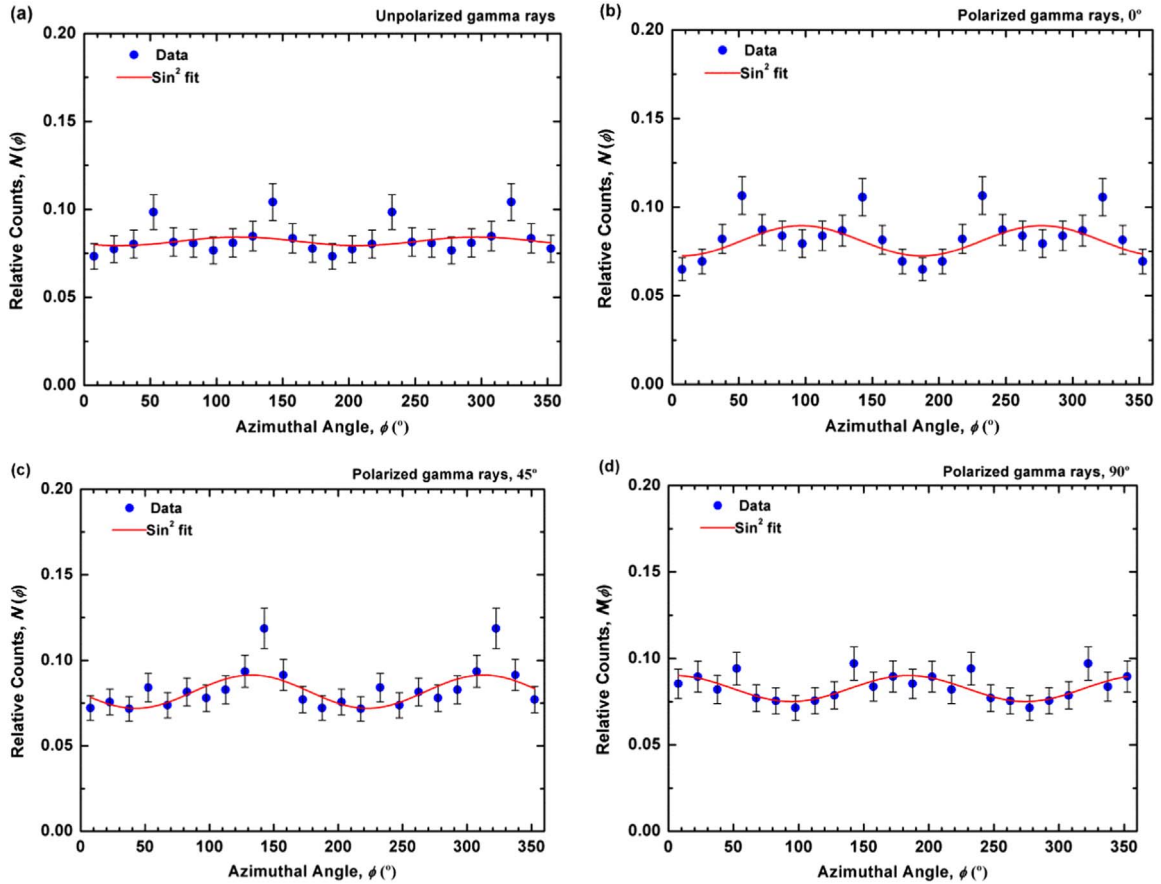


Fig. 6. Flowchart of the polarimetric measurement detector hits' analysis implemented on a MatLab based code.



**Fig. 7.** Double-event intensity maps obtained for an aluminum target polarizer for  $0^\circ$  (left),  $45^\circ$  (middle) and  $90^\circ$  (right) detector prototype rotation. The acquisition time for each measurement was of  $2 \times 10^5$  s.



**Fig. 8.** (a) Residual modulation obtained after matrix prototype irradiation with an unpolarized gamma-ray beam with 511 keV. (b) Modulation obtained with the aluminum target when detector prototype rotation is oriented at  $0^\circ$ , (c) at  $45^\circ$  and (d) at  $90^\circ$ . The fitting curves in red are represented just for guideline purposes. (For interpretation of the references to color in this figure legend, the reader is referred to the web version of this article.)

**Table 2**

Measured angle and level of polarization and the respective modulation factor  $Q$  for an aluminum target.

Detector rotation angle (deg)	Measured angle (deg)	Modulation factor $Q$	Polarization level (%)
0	$12.0 \pm 5.8$	$0.117 \pm 0.018$	$39.0 \pm 6.0$
45	$33.3 \pm 9.5$	$0.118 \pm 0.019$	$39.3 \pm 6.3$
90	$97.5 \pm 4.3$	$0.116 \pm 0.009$	$38.6 \pm 3.0$

number of double-events are counted. Consequently, the uncertainty increases when calculating the angular polarization direction for these poorer statistic pixels.

## 6. Conclusions

Experimental tests and simulations of complex conditions similar to operational conditions of a space spectro-imager polarimeter provide valuable information on the instruments' response which might be determinant to its design and development. Herein, instead of irradiation conditions such as central matrix pixel scatterer or scatterer-calorimeter configurations we irradiated a large active detection surface ( $1 \text{ cm}^2$ ) where all the detection units (pixels) operated simultaneously as a scatterer and as an absorber. This prototype was also operated under a low level partially polarized beam. Both operation conditions are closer to inflight conditions than those in previous experiments. Simultaneous CZT multiple pixel irradiation required analysis tools based on Compton scattering kinematics and rely on the

spectrometer detector capabilities. The  $7 \times 7$  virtual matrix method applied to our measurements allowed to appropriately analyze the double-events distributions generated in a full irradiated  $4 \times 4$  matrix. A  $\sim 40\%$  average linearly polarized beam was measured as well as its polarization angle with a good precision (error within  $\pm 5^\circ$  to  $\pm 9^\circ$ ) for a small 16 pixel matrix rotated at different detector angles ( $0^\circ$ ,  $45^\circ$  and  $90^\circ$ ). These results emphasize the fine potential of CZT based polarimeters operating under low flux, low polarization and complex inflight conditions.

## 7. Acknowledgment

R.M. Curado da Silva thanks to the Fundação Luso-Americana, Portugal, for supporting the travel expenses (ref. 203/2014) to present this work at the IEEE 21st Symposium on Room Temperature Semiconductor Detectors, Seattle, USA, 2014. We thank Benilde F.O. Costa of Department of Physics, University of Coimbra, 3004-516 Coimbra, Portugal, as well as ICNAS (Instituto de Ciências Nucleares Aplicadas à Saúde) Universidade de Coimbra, 3000-548 Coimbra, Portugal, for providing material resources that allowed to accomplish this work. Manuscript received November 6, 2015. The work of R.M. Curado da Silva was supported by the FCT Ciência program. The work of L. Pereira was supported by FCT grant SFRH/BD/82505/2011.

## References

- [1] F. Lei, A.J. Dean, G.L. Hills, Compton polarimetry in gamma-ray astronomy, *Space Sci. Rev.* 82 (1997) 309–388.
- [2] R. Bellazzini, et al., *X-ray Polarimetry: A New Window in Astrophysics*, Cambridge University Press, Cambridge, United Kingdom, 2010.
- [3] Mark McConnell et al., X-Ray and gamma-ray polarimetry, *Astro2010: The Astronomy and Astrophysics Decadal Survey*, Science White Papers, no. 198, 2009.
- [4] R. Novick, M.C. Weisskopf, R. Berthelsdorf, et al., Detection of X-ray polarization of the Crab Nebula, *Astrophys. J.* 174 (1972) L1.
- [5] M.C. Weisskopf, et al., A precision measurement of the X-ray polarization of the Crab Nebula without pulsar contamination, *Astrophys. J.* 220 (1978) L117.
- [6] E. Suarez-Garcia, W. Hajdas, Polarimetry at high energies, observing photons in space, Vol. 9, ISSI Scientific Report Series, pp. 599–615.
- [7] E. Suarez-Garcia, W. Hajdas, POLAR: design of a novel X-ray polarimeter based on plastic scintillators and MAPMTs, *Nucl. Instrum. Methods A* 610 (2009) 276–279.
- [8] Y. Kishimoto, Basic performance of PHENEX: a polarimeter for high energy X rays, *IEEE Trans. Nucl. Sci.* 54 (3) (2007) 561–566.
- [9] H. Krawczynski, A. Garson III, J. Martin, et al., The hard X-ray polarization sensitivity of the energetic X-ray imaging survey telescope EXIST, *PoS(CRAB2008)* 026.
- [10] J.E. Hill, M.L. McConnell, P. Bloser, et al., POET: Polarimeters for Energetic Transients, *AIP Conference Proceedings*, vol. 1065, pp. 331, 2008.
- [11] J. Greiner, A. Iyudin, G. Kanbach, Gamma-ray burst investigation via polarimetry and spectroscopy (GRIPS), *Exp. Astron.* 23 (1) (2009) 91–120.
- [12] H. Tajima, R. Blandford, T. Enoto, et al., Soft Gamma-ray Detector for the ASTRO-H Mission, in: *Proceedings of the SPIE*, Volume 7732, 2010, pp. 773216–773217.
- [13] D. Yonetoku, T. Murakami, S. Gunji, Gamma-ray burst polarimeter - GAP - aboard the small solar power sail demonstrator IKAROS, *Astron. Soc. Jpn.* 63 (2011) 625.
- [14] T. Kamae, et al., PoGoLite – a high sensitivity balloon-borne soft gamma-ray polarimeter, *Astropart. Phys.* 30 (2008) 72–84.
- [15] C. Winkler, T.J. Courvoisier, et al., The integral mission, *Astron. Astrophys.* 411 (2003) L1–L6.
- [16] P. Ubertini, F. Lebrun, G. Di Cocco, et al., IBIS: the Imager on-board INTEGRAL, *Astron. Astrophys.* 411 (2003) L131–L139.
- [17] A.J. Dean, et al., Polarized gamma ray emission from the CRAB, *Science* 321 (5893) (2008) 1183–1185.
- [18] M. Forot, et al., Polarization of the crab pulsar and nebula as observed by the INTEGRAL/IBIS telescope, *Astrophys. J.* 688 (2008) L29–L32.
- [19] P. Laurent, J. Rodriguez, J. Wilms, et al., Polarized gamma-ray emission from the galactic black hole cygnus X-1, *Science* 332 (6028) (2011) 438–439.
- [20] D. Götz, P. Laurent, F. Lebrun, et al., Variable polarization measured in the prompt emission of GRB 041219A using IBIS on board INTEGRAL, *Astrophys. J. Lett.* 695 (2009) 2.
- [21] J. Knödseder, et al., GRI: focusing on the evolving violent universe, in: S.L. O'Dell, G. Pareschi (Eds.), *Proceedings of SPIE on Optics for EUV, X-Ray, and Gamma-Ray Astronomy III*, 2007, vol. 6688, pp. 668806.
- [22] P. von Ballmoos, T. Takahashi, S.E. Boggs, A DUAL mission for nuclear astrophysics, *Nucl. Instrum. Methods A* 623 (2010) 431–433.
- [23] M. Tavani et al., The ASTROGAM Mission, in: *Second ASTROGAM Workshop*, LPNHE, Paris, France, March 26–27, 2015.
- [24] R.M. Curado da Silva, E. Caroli, J.B. Stephen, P. Siffert, CIPHER, a polarimeter telescope concept for Hard X-ray Astronomy, *Exp. Astron.* 15 (1) (2003) 45–65.
- [25] A. Zoglauer, C.B. Wunderer, G. Weidenspointner, E. Caroli, R.M. Curado da Silva, S.E. Boggs, J. Knödseder, Simulated Performance of CZT-based Focal Plane Detectors for Gamma-Ray Lenses, in: *2006 IEEE Nuclear Science Symposium Conference Record*: 3742–3749, 11/2006.
- [26] P.F. Bloser, J.S. Legere, M.L. McConnell, et al., Calibration of the gamma-ray polarimeter experiment (GRAPE) at a polarized hard X-ray beam, *Nucl. Instrum. Methods A* 600 (2009) 424.
- [27] R.M. Curado da Silva, E. Caroli, N. Auricchio, et al., Hard-X and soft gamma-ray polarimetry with CdTe array prototypes, *IEEE Trans. Nucl. Sci.* 51 (5) (2004) 2478–2484.
- [28] R.M. Curado da Silva, et al., Polarimetric performance of a Laue lens gamma-ray CdZnTe focal plane prototype, *J. Appl. Phys.* 104 (8) (2008) 084903.
- [29] Ezio Caroli, Rui M. Curado da Silva, John B. Stephen, et al., A polarimetric experiment with a laue lens and CZT pixel detector, *IEEE Trans. Nucl. Sci.* 56 (4) (2009) 1848–1854.
- [30] R.M. Curado da Silva, N. Auricchio, E. Caroli, et al., Polarimetry study with a CdZnTe focal plane detector, *IEEE Trans. Nucl. Sci.* 58 (4) (2011) 2118–2123.
- [31] R.M. Curado da Silva, E. Caroli, J.B. Stephen, N. Auricchio, J.M. Maia, et al., Polarization degree and direction angle effects on a CdZnTe focal plane performance, *IEEE Trans. Nucl. Sci.* 59 (4) (2012) 1628–1635.
- [32] S. Antier, P. Ferrando, O. Limousin, E. Caroli, R.M. Curado da Silva, et al., Hard X-ray polarimetry with Caliste, a high performance CdTe based imaging spectrometer, *Exp. Astron.* 39 (2) (2015) 233–258.
- [33] Mark L. McConnell, James Ledoux, John Macri, James Ryan, Dedicated polarimeter design for hard x-ray and soft gamma-ray astronomy, in: *Proceedings. SPIE 5165, X-Ray and Gamma-Ray Instrumentation for Astronomy XIII*, 334, 2004.
- [34] R.A. Kroeger, W.N. Johnson, J.D. Kurfess, B.F. Philips, “Gamma ray polarimetry using a position sensitive germanium detector, *Nucl. Instrum. Methods A* 436 (1999) 165.
- [35] R.A. Kroeger, W.N. Johnson, R.L. Kinzer, et al., Gamma-Ray Instrument for Polarimetry, Spectroscopy and Imaging (GPSI), in: *Proceedings. SPIE 2806, Gamma-Ray and Cosmic-Ray Detectors, Techniques, and Missions*, 52, 1996.
- [36] T. Chattopadhyay, S.V. Vadawale, A.R. Rao, S. Sreekumar, D. Bhattacharya, Prospects of hard X-ray polarimetry with Astrosat-CZTI, *Exp. Astron.* 37 (2014) 555–577.
- [37] S.V. Vadawale, T. Chattopadhyay, A.R. Rao, Hard X-ray polarimetry with Astrosat-CZTI, *Astron. Astrophys.* 578 (2015) A73.
- [38] S. Takeda, H. Odaka, J. Katsuta, et al., Polarimetric performance of Si/CdTe semiconductor Compton camera, *Nucl. Instrum. Methods A* 622 (3) (2010) 619–627.
- [39] M. Suffert, P.M. Endt, A.M. Hoogenboom, Polarization measurements of proton capture gamma rays, *Physica* 25 (1959) 659.
- [40] J.H. Hubbel, S.M. Seltzer, Tables of X-ray mass attenuation coefficients and mass energy-absorption coefficients 1 keV to 20 MeV for elements Z=1 to 92 and 48 additional substances of dosimetric interest, *NISTIR* 5632 (1995).
- [41] J.E. Naya Ariste, F. Alberne, G. Vedrenne, Computer simulation of an array of Ge detectors for  $\gamma$ -ray imaging, *Nucl. Instrum. Methods A* 357 (1995) 170–177.
- [42] MATLAB version 7.10.0. Natick, The MathWorks Inc.: Massachusetts, 2010.
- [43] S. Agostinelliae, J. Allisonas, K. Amako, Geant4 - a simulation toolkit, *Nucl. Instrum. Methods A* 506 (2003) 250–303.